ADVANCED FUNCTIONAL MATERIALS
www.afm-journal.de

Dual-Polarized Broadband Laplace Differentiator via Quasi-Bound States in the Continuum Empowered by Nonlocal Metasurfaces

Chen Zhou, Ruizhe Zhao, Peijin Li, Yan Zhang, Yanjie Chen, Guangzhou Geng, Junjie Li, Xiaowei Li, Yongtian Wang, and Lingling Huang**

Directly performing optical analog computations and image processing in space, such as optical differential operations and image edge detection, is a burgeoning area. To avoid the bulkiness and low efficiency of traditional 4*f* filtering systems, one can utilize Green's function and metasurfaces for advanced wavefront control. However, some metasurface differentiators can be hindered by issues like polarization sensitivity, restricted bandwidth, low resolution, and the need for additional polarization devices or digital post-processing, potentially degrading their performance and operation efficiency. In this work, a dual-polarization Laplace differentiator is engineered to address these issues based on nonlocal hollow metasurface. The optical transfer function (OTF) required by the Laplace operation can be obtained by exciting different quasi-bound states in the continuum (Q-BIC) modes with distinct angular dispersion capabilities under *p*- and *s*-polarized illumination, respectively. This Laplace differentiator not only directly realizes 2D second-order edge detection in a dual-polarization channel but also features a numerical aperture (NA) with an upper limit close to 0.42 and a broadband range reaching 165 nm. Such an efficient, high-quality dual-polarization and bandwidth image edge detection approach offers powerful imaging techniques for applications in machine vision, microscopic imaging, and image processing.

1. Introduction

Compact and efficient optical analog computing platform plays a key role to implement image processing, particularly important in autonomous driving and machine vision.[1–4] This approach also provides significant advantages in medical imaging and head-mounted display applications.[5–9] In contrast to conventional digital differentiators, optical analog differentiators harness device-specific transfer functions to differentiate incident light, capturing high frequency components of the incident optical field and filtering out low ones. Optical spatial analog differentiation is usually done using Fourier spatial filtering methods and Green's function methods.[10] No matter which method is used, the core purpose is to make the device have an optical transfer function (OTF) to perform differential operations.[11] In the former, it mainly relies on a 4*f* filtering system. Subsequently, a spatial frequency mask is applied in the frequency domain to obtain the differentiated image.[12,13] However, such bulky 4*f* systems hinder miniaturization and integration into existing commercial imaging systems. The latter approach focuses on designing an OTF with angular dispersion response to the incident field and performs edge detection directly in the spatial domain.[10] By eliminating the need for a 4*f* system's lens assembly, it achieves a more compact differential image processing system, simplifying the complexity and promoting scalability for integrated applications.

For traditional optical devices, designing an OTF with angular dispersion response for implementing optical analog

C. Zhou, R. Zhao, P. Li, Y. Zhang, Y. Chen, Y. Wang, L. Huang
Beijing Engineering Research Center of Mixed Reality and Advanced Display
MIIT Key Laboratory of Photonics Information Technology
School of Optics and Photonics
Beijing Institute of Technology
Beijing 100081, China
E-mail: wyt@bit.edu.cn; huanglingling@bit.edu.cn

C. Zhou, R. Zhao, P. Li, Y. Zhang, Y. Chen, Y. Wang, L. Huang
National Key Laboratory on Near-surface Detection
Beijing 100072, China

G. Geng, J. Li
Beijing National Laboratory for Condensed Matter Physics
Institute of Physics
Chinese Academy of Sciences
Beijing 100191, China

X. Li
Laser Micro/Nano-Fabrication Laboratory
School of Mechanical Engineering
Beijing Institute of Technology
Beijing 100081, China

The ORCID identification number(s) for the author(s) of this article can be found under https://doi.org/10.1002/adfm.202426095

DOI: 10.1002/adfm.202426095

differentiation via Green's function method is extremely challenging. Fortunately, the advancement of metasurface technology significantly ameliorates this issue.[14–16] As an ultrathin artificial engineered structure, metasurfaces can precisely control the amplitude, phase, and polarization of incident fields at the micro- and nano-scales.[17–21] Consequently, they offer significant advantages and broad application prospects in wavefront manipulation,[22–25] holography,[26–28] precision measurement,[29,30] optical analog computing and image processing.[31–33] Meanwhile, it overcomes the bulkiness, energy inefficiency, and slow processing of digital and traditional analog image processing, facilitating high-throughput parallel processing. Experiments demonstrate that metasurface differential operators can achieve unidirectional first-order differential operations and edge detection through surface plasmon resonance, photonic spin Hall effect, and the Pancharatnam-Berry phase.[34–36] However, generally speaking, to obtain all of the edge contour information from a 2D image, the simplest method is to design a Laplacian differentiator, which can exhibit the effect of two dimensions second-order image edge detection.[37] The Laplacian operator is a fundamental tool in image processing for detecting edges and textures within an image. Mathematically, it operates by applying second-order partial derivatives to the image. Physically, however, it effectively highlights regions where there is a significant change in pixel values, which typically occurs at the edges of images. Therefore, based on Green's function method, an effective strategy to achieve the OTF required for Laplace differential operation is to design nonlocal metasurfaces with angle selectivity for the incident light field.[38,39] Here, "nonlocal" denotes collective resonances featuring significantly extended electric fields and strong metaunit interactions, while the corresponding "local" refers to quasi-isolated site resonances with localized electric fields and minimal interaction among metaunits.[40]

Compared to conventional glass lenses having OTF defined in real space, nonlocal metasurface have OTF modulated purely in *k*-space due to translation symmetry, which corresponds to a multiplication operator in the *k*-space rather than in real space.[41,42] Consequently, nonlocal metasurfaces sensitive to the incident angle can be engineered to facilitate the execution of optical analog differential operations and edge detection. For instance, nonlocal metasurfaces can excite Fano resonances, guide mode resonances, or Mie resonances, which can provide the necessary OTF for Laplace differential operations.[43–52] However, some metasurface Laplace differentiators of these schemes face limitations. Such as, some differentiators only perform in theoretical designs that are not practically fabricable. Moreover, some differentiators can be hindered by issues with polarization sensitivity, restricted narrow bandwidth, low resolution, and the requirement for extra polarization devices or digital post-processing. Above mentioned schemes can potentially degrade their performance and operational efficiency. Consequently, designing a Laplacian differentiator that operates across dual-polarization channels, broad bandwidths, and has a large angular dispersion response (or large NA) remains challenging. Currently, photonic crystal slabs with C_6 lattice symmetry can perform Laplacian differentiation in single or dual-polarization channels.[53,54] Nevertheless, achieving higher NA and broader bandwidth Laplacian differentiation or 2D second-order edge detection in dual-polarization channels using C_4 lattice structures remains challenging.

In this work, we design a single-layer dielectric silicon nonlocal hollow metasurface with a square cavum structure that exhibits Laplace differential operations with a certain bandwidth range under *p*- and *s*-polarized in the near-infrared band, respectively. Its dual-polarization broadband Laplace differentiator characteristics rely on the excitation of quasi-bound state in the continuum (Q-BIC). The concept of BIC or Q-BIC is demonstrated with exotic optical properties, such as perfect absorption, high-Q devices, and polarization vortex generation, among others.[55–65] The highly symmetric structure of the square hollow structure is beneficial for obtaining a nearly isotropic OTF required for Laplacian operations. Notably, under *p*-polarization, the Q-BIC mode is primarily dominated by magnetic dipole resonance. Meanwhile, this characteristic enables Laplace differentiation and 2D second-order image edge detection with the NA increases from 0.24 to 0.39 within the range of 1325 to 1400 nm, while for wavelengths from 1425 to 1450 nm, the NA upper limit reaches 0.42. Experimentally, the broadband edge detection results can be further extended to 165 nm. Under *s*-polarization, the excited Q-BIC mode is mainly governed by magnetic quadrupole resonance. Within the spectral range of 1270 to 1300 nm, it can also efficiently and in real space achieve Laplacian differentiation and 2D second-order image edge detection with the NA ranging from 0.17 to an upper limit of 0.42. This work presents the nonlocal hollow metasurface Laplace differentiator with a dual polarization channel in transmission mode at broadband wavelengths and without relying on the 4*f* filtering system. Such a scheme provides a platform for optical analog computing in image processing applications such as biochemical medical imaging and machine vision.

2. Results and Discussion

2.1. Principle of the Dual-Polarization Laplace Differentiator

According to the principles of optical imaging, any mathematical operation defined in Fourier space can be performed by selectively filtering the spectral components emanating from the image along the different directions of light wave propagation.[12] To directly realize image edge detection and recognition in all directions of an image in the spatial domain without relying on the 4*f* filtering system, the most straightforward method is to design the metasurface to perform as the Laplace differential operator. It is the simplest isotropic differential operator in 2D image processing and can obtain 2D second-order edge detection results. For natural materials it is difficult to perform complex wavefront processing directly in real space, hence one can just encode the required mathematical operations into the OTF within the metasurface. As the incident field with an electric field profile $E_{in}(x,y)$ passes through the Laplace differential metasurface, the outgoing field is $E_{out}(x,y) \propto (\partial^2/\partial x^2 + \partial^2/\partial y^2) E_{in}(x,y)$. Where $\nabla^2 = (\partial^2/\partial x^2 + \partial^2/\partial y^2)$ represents the Laplace operator.

If one aims to design a Laplacian differential operator that does not operate in a single polarization state, one can design a metasurface that performs Laplacian differentiation under both *p*- and *s*-polarization, as shown in **Figure 1**. At this point, the OTF of the

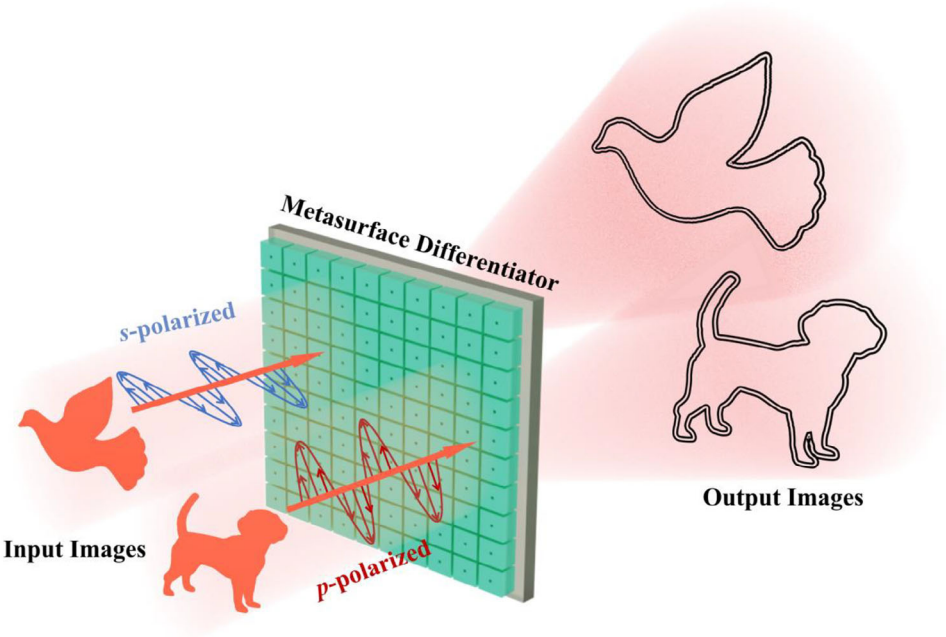

Figure 1. Schematic diagram of the implementation of the Laplace differentiator based on a nonlocal hollow metasurface via quasi-bound states in the continuum under a dual-polarization channel. The all-directional 2D second-order edge detection results are obtained for the incident fields of a dog and a dove under *p*- and *s*-polarized through the metasurface differentiator, respectively.

designed metasurface must mathematically satisfy the following expression:[66]

$$t(k_{||}) = \begin{bmatrix} t_{ss}(k_{||}) & t_{sp}(k_{||}) \\ t_{ps}(k_{||}) & t_{pp}(k_{||}) \end{bmatrix} = \begin{bmatrix} c_{ss}t_{ss}(\theta,\varphi) & 0 \\ 0 & c_{pp}t_{pp}(\theta,\varphi) \end{bmatrix} \quad (1)$$

where the subscripts s and p denote the polarization of the incident and transmitted beams, respectively. $k_{||} = k\sin(\theta)$, k is the incident wavevector. θ and φ are the polar angles and azimuthal angles, respectively. On the other hand, $k_{||}^2 = k_x^2 + k_y^2$ denotes the in-plane wave vector. Therefore, it can be inferred that the OTF of the metasurface designed to perform Laplacian differentiation in both polarization states should satisfy a quadratic relationship with the wave vector, reflecting the second derivative nature of the Laplacian operator. From the physical perspective, regardless of whether *p*- or *s*-polarized light is incident, this corresponds to the designed metasurface having zero transmittance under normal incidence and transmittance should satisfy a quadratic relation at oblique incidence.

In practical applications, when implementing a Laplacian differential operator for dual-polarization operation, two important metrics about the efficiency and resolution of image edge detection also need to be considered. To achieve the highest efficiency, the designed metasurface differential operator should have a transmission amplitude as large as possible at the maximum incident wave vector, ideally being unity. In addition, the largest incident wavevector defines the largest incident angle, which directly affects the NA of the differentiator, and consequently, the actual resolution. Therefore, designing a metasurface differentiator that depends on a sufficiently large incident angle not only allows for a sufficiently large NA, which directly affects the resolution of the metasurface differentiator, but also facilitates direct integration into existing commercial imaging systems, enriching and improving the image processing capabilities and efficiency.

2.2. Design of Metasurface

According to Equation (1), the OTF of the designed metasurface has no transmittance under normal incidence and the transmittance needs to increase as the incident angle increases in *p*- and *s*-polarization channels. It is necessary for the metasurface to function properly for these two orthogonal polarizations over a certain wave vector range. In other words, the metasurface can be considered a high-pass filter. Commonly, such optical properties can be achieved not only through typical resonances, such as electric dipole resonance, magnetic dipole resonance, or toroidal dipole resonance, but also through the excitation of Q-BICs in nonlocal metasurfaces. It provides a new degree of freedom to design the optical filters and differentiators.

Typically, BICs that arise from metasurfaces are classified into two categories: symmetry-protected BICs and accidental BICs. For symmetry-protected BICs, under normal incidence conditions, the metasurface cannot couple with light in free space, resulting in non-radiative dark state modes. This leads to the amplitude value of reflected or transmitted light spectra being zero or nearly zero. Such characteristics can be utilized to filter out low-frequency information from images. As the normal incident field transitions to oblique incidence, the symmetry of the overall system constituted by nonlocal metasurfaces is broken. Without altering the inherent symmetry of the structure, the non-radiative BIC can be excited into a Q-BIC capable of coupling with free space. Consequently, this allows the excitation of light beams confined at specific frequencies within the structure, manifesting as

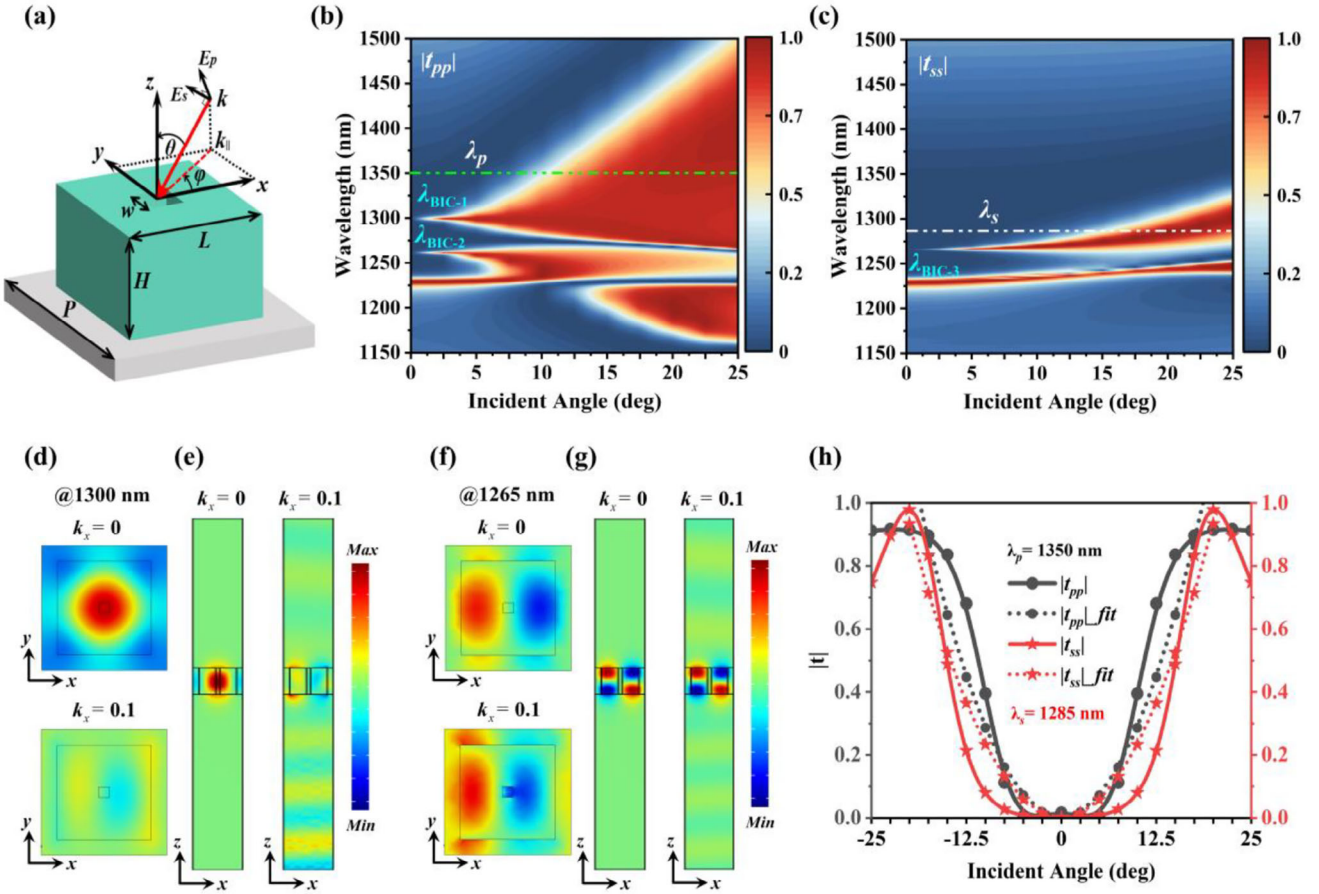

Figure 2. Parameters and resonance characters of the dual-polarization Laplace differentiator. a) Schematic of a unit cell of the dielectric metasurface and incident source, where θ and φ are the incidence and azimuthal angle, respectively. b,c) Transmission spectra as a function of different incident angles for *p*- and *s*-polarized under azimuthal angle $\varphi = 0°$, respectively. d) Top views of the Ez field profiles showing excitation of the BIC (top) and quasi-guided mode (bottom) at $k_x = 0$ and $0.1(2\pi/P)$ at 1300 nm, respectively. e) Side views of the Ez field profiles showing excitation of the BIC (left) and quasi-guided mode (right) at $k_x = 0$ and $0.1(2\pi/P)$ at 1300 nm, respectively. f) Top views of the Hz field profiles showing excitation of the BIC (top) and quasi-guided mode (bottom) at $k_x = 0$ and $0.1(2\pi/P)$ at 1265 nm, respectively. g) Side views of the Hz field profiles showing excitation of the BIC (left) and quasi-guided mode (right) at $k_x = 0$ and $0.1(2\pi/P)$ at 1265 nm, respectively. h) Transmission amplitudes and corresponding fits at 1350 nm and 1285 nm for *p*- and *s*-polarized in oblique illumination, respectively.

an increase in transmission amplitude in the spectrum. As long as the designed metasurface maintains a continuous increase in the transmission spectrum amplitude over a sufficiently large range of oblique incidence angles for specific wavelengths under both *p*- and *s*-polarizations, and satisfies a quadratic relationship. It can be utilized to implement Laplacian differential operations and broadband 2D second-order image edge detection in dual-polarization states.

With the aim of realizing BICs or Q-BICs for the incident fields at large wave vectors under both *p*- and *s*-polarization, the exploration of suitable metasurface structures and parameters is important. Based on the theoretical study of dielectric silicon nonlocal hollow metasurface, we find that by designing the appropriate parameters of hollow bricks, it is possible to regulate the distribution of electromagnetic field energy within a low refractive index space or localized inside the dielectric column. Additionally, the hole in the hollow brick allows a strong electromagnetic field to leak from the dielectric into the free space. This enables the acquisition of a variety of distinct resonance modes, which aid in achieving angle-selective BICs or Q-BICs in *p*- or *s*-polarized channels. Therefore, we choose amorphous silicon to design a nonlocal metasurface placed on a glass substrate to realize the Laplace differential operation and correspondingly edge detection functions, as shown in **Figure 2a**. Simultaneously, it's expected that the metasurface has those Q-BIC modes that are sensitive to a large oblique incidence angle and have the potential for broadband application. Finally, such a unit cell consisting of the silicon hollow brick is obtained with a thickness of H = 450 nm and a glass substrate with a refractive index of 1.45. The lattice period is P = 600 nm, the outer square edge length is L = 450 nm, and the center square hole edge length is w = 50 nm. It is worth noting that the transmission light of such a designed structure will not undergo polarization conversion. Meanwhile, the symmetry of the nonlocal metasurface is beneficial to maintain the isotropic OTF in the in-plane direction.

2.3. Transmittance Spectra of Metasurface

For a clear understanding of the relationship between the transmission spectra of the designed nonlocal hollow metasurface under different polarization conditions and the incidence angle, the following results are presented. The transmission of *p*- and *s*-polarized are simulated as a function of wavelength in the near-infrared spectral region from 1150 to 1500 nm, and incidence angle for the range of the maximum oblique incidence angle θ_{max} up to 25° when the azimuthal angle φ= 0°are shown in Figure 2b,c, respectively.

At normal incidence, the designed nonlocal metasurface exhibits a Fano resonance peak dominated by a toroidal dipole resonance at 1230 nm, with a transmission amplitude close to unity (for details, see Section S1, Supporting Information). Simultaneously, within the range from 1250 to 1350 nm, it provides an extremely low transmission value with a broadband of ≈100 nm, which is essentially close to zero. This establishes the foundational prerequisite for the metasurface to act as a Laplace differential operator by blocking low spatial frequency information. However, at oblique incidence, the transmission and angular dispersion responses follow different trends for *p*- and *s*-polarization. Most notably, for the *p*-polarized channel, there exist two BICs at 1300 and 1260 nm, labeled as BIC-1 and BIC-2 in Figure 2b. For the *s*-polarized channel, only a single BIC is present at 1265 nm, labeled as BIC-3 in Figure 2c. These BICs are completely decoupled from free space due to symmetry protection under normal incidence. Under *p*-polarization, as shown in Figure 2b, as the incident angle increases from 0° to 25°, the BIC-1 and BIC-2 resonances at 1300 and 1260 nm begin to couple with free space, transforming into quasi-guide modes with finite lifetimes, known as Q-BICs. Concurrently, the increase in the incident angle leads to rapid changes in the Fano resonance line shapes in the transmission spectra. At 1260, BIC-2′s maximum transmission value approaches unity at an oblique angle ≈10° (for details, see Section S2, Supporting Information). In pursuit of achieving the largest possible NA for a Laplace differential operator, this paper primarily investigates the resonance characteristics of BIC-1. As the oblique incidence angle increases, the transmission spectrum of BIC-1 at 1300 nm exhibits significant broadening, which is favorable for demonstrating its broadband operational capability. Meanwhile, the transmission amplitude gradually increases in a gradient manner within the range from 1300 to 1500 nm. This is beneficial for achieving Laplace differential operations. Under *s*-polarization, as depicted in Figure 2c, the BIC-3 resonance at 1265 nm begins to couple with free space and becomes a Q-BIC with a finite lifetime as the incidence angle increases from 0° to 25°. Similarly, the transmission intensity exhibits a gradient increase from 1265 to 1300 nm, which is also conducive to providing a foundation for Laplace differential operation.

To better understand the resonance characteristics of BIC-1 and BIC-3 under *p*- and *s*-polarized illumination, we investigate their mode profiles as a function of the in-plane wavevector. The structure is modeled using the Finite Element Method (for details of the simulation, see Methods). For BIC-1, Figure 2d,e displays the distribution of the E_z field profile. The BIC-1 at the Γ point is protected by the symmetry of the unit cell. This can be observed by examining the mode pattern at the top of Figure 2d. The normal component of the modal electric field is shown at the top panel, the near-field distribution is symmetric (even) under a 180° rotation around the normal direction of the metasurface, whereas the plane waves exhibit antisymmetric (odd) behavior under the same operation. For a system with a sub-diffractional period, the array of dipoles oscillates in phase, supporting in-plane radiation completely decoupled from free space. Therefore, BIC-1 cannot radiative to free space at the Γ point, as illustrated on the left side of Figure 2e. Away from the Γ point, the symmetry of the entire system is broken, and the state of BIC-1 begins to transform into a quasi-guided mode and radiative, namely Q-BIC-1. This can be observed from the bottom of Figure 2d and the side view of the Ez field distribution on the right side of Figure 2e. Based on symmetry considerations, nonlocal metasurfaces only couple with free-space modes of the same type of symmetry. Thus, Q-BIC-1 can only be excited by *p*-polarization, leading to angle-selective transmission under *p*-polarization, and it is revealed as a magnetic dipole resonance in the transmission spectrum at 1300 nm. For BIC-3, Figure 2f,g displays the distribution of the Hz field profile. The modes displayed at the top of Figure 2f and on the left of Figure 2g indicate that BIC-3 is also symmetrically protected at the Γ point and unable to radiate to free space. However, unlike BIC-1, BIC-3′s normal magnetic field component indicates that it is an odd mode. While the side view mode exhibits an odd mode, it also possesses 180° rotational symmetry. As away from the Γ point, this BIC-3 state starts to become quasi-guided mode and radiative as the symmetry is no longer protected, namely Q-BIC-3, which can be observed from Figure 2f (below) and Figure 2g (right). Hence, the Q-BIC-3 can only be accessed by the *s*-polarization with an incident angle and manifests a magnetic quadrupole resonance at the transmission spectrum at 1265 nm.

Next, it is necessary to continue to investigate the precise relationship between the transmittance coefficient and the incidence angles under different polarization conditions. To achieve the purpose of Laplace differential operation, it is necessary to select the working wavelength away from BIC. As shown in Figure 2b,c, we choose λ_p (1350 nm) and λ_s (1285 nm) as the working wavelengths for the *p*- and *s*-polarized channels to obtain the appropriate OTF, respectively. Their corresponding fitting results are shown in Figure 2h. It can find that the transmission amplitude and oblique incidence angle of the nonlocal hollow metasurface satisfy the quadratic relationship in these two orthogonal polarization states, which provide the necessary conditions to realize the Laplace operation for the dual-polarization channel. From Figure 2h, it can be observed that the maximum fitting value of the quadratic curve of the $\lambda_p$and λ_s can reach NA = 0.31 and NA = 0.33, which indicates the edge detection resolution ($0.61 \cdot \lambda/NA$) of this Laplace differentiator can reach 2.656 and 2.375 μm for the *p*- and *s*-polarized channel, respectively. Furthermore, the spectra based on the resonant positions of Q-BIC-1 and Q-BIC-3 exhibit broadening with the increase of the oblique incidence angle, and the fitting of the OTFs at more wavelengths are studied respectively (for details, see Sections S3 and S4, Supporting Information). It can be observed that this nonlocal hollow metasurface differentiator achieves an NA upper limit of 0.42 at 1425 nm under p-polarization and at 1300 nm under s-polarization. Although standard Laplacian operations cannot be performed at these wavelengths, second-order differentiation can still be executed at selected azimuthal angles. Theoretically, the

corresponding maximum resolutions are 2.033 and 1.888 μm, respectively, both of which are equivalent to 1.45 times to their respective wavelengths. Therefore, based on the preliminary analysis, the designed nonlocal hollow metasurface has the potential to achieve boardband image edge detection with dual polarization channels, large NA and high resolution.

2.4. Broadband isotropy OTF of Metasurface

According to the definition of the Laplace differential operator, it is also required that the angle-dependent OTFs satisfy the independence of different azimuthal angles. For this reason, the transmission spectra and phases of incident light at different wavelengths are simulated for different azimuthal angles in *p*- and *s*-polarized light for arbitrary wave vectors, as shown in **Figure 3**. During the simulation, the incident light of different polarization states with the incident angle θ is set from 0° to 25° in 5° steps, and the azimuth angle φ is also set in 5° steps from 0° to 360°.

Based on the 2D transmission angular dispersion spectra of the nonlocal hollow metasurface depicted in Figure 3, the 2D OTFs for *p*- and *s*-polarization at different wavelengths exhibit approximately isotropic contours. As observed in Figure 3a–f, under the *p*-polarization channel, the 2D OTFs from 1325 to 1400 nm exhibit a well-defined isotropic contour. This indicates that within this wavelength band, the transmission amplitude of the designed metasurface is insensitive to changes in azimuthal angle, thereby maintaining azimuthal independence for the transmission spectrum of any incident wave vector. This characteristic is beneficial for processing 2D information in a single shot. From the range of 1400 to 1450 nm, it can be observed that the 2D OTFs corresponding to the respective wavelengths still exhibit approximately uniform contours, despite the presence of the non-zero phenomenon within the small incidence angle. This can lead to the inability of the metasurface to fully filter out low-frequency image information, resulting in some residual background noise. Nevertheless, as the angle of oblique incidence increases further, image information with high-frequency components can be rapidly and efficiently transmitted, thereby still allowing for a distinct edge detection to be observed. This result will be evident in the subsequent imaging experiments. For the *s*-polarization channel, built upon the analysis of Figure 3g–l, it can be observed that the 2D OTFs within the wavelength range of 1270 to 1300 nm are also basically insensitive to changes in azimuthal angle. Moreover, as the wavelength increases, the rotational symmetry of these OTFs improves, demonstrating the isotropic characteristics required for Laplace differential operation under broadband *s*-polarization.

Additionally, an analysis is conducted on the random phase distributions corresponding to the 2D OTFs for all *p*- and *s*-polarized light presented in Figure 3 (for details, see Section S5, Supporting Information). The results indicate that within the designed range of incident angles, the nonlocal hollow metasurface can provide a uniform and stable phase distribution for any incident wave vector at an arbitrary azimuthal angle. Consequently, the OTFs of the designed metasurface at various wavelengths for both *p*- and *s*-polarization can adhere to the criteria of the Laplacian operation. It possesses the capability for real-time, broadband, high-resolution, and azimuthally independent (or isotropic) 2D second-order edge detection in dual-polarization channels. Meanwhile, it needs to be emphasized that this strategy eliminates the need for a 4*f* filtering system or extra optical components, making the optical analog image processing system more compact. This compactness allows for integration into both traditional and non-traditional imaging systems, achieving a true minimization of the imaging system.

2.5. Sample Fabrication and Imaging Experiment

According to the original design of the nonlocal hollow metasurface differentiator, after the light field of the target passes through it, the transmit light is directly modulated in the spatial domain, and then the 2D second-order edge information of the target object can be directly observed. To experimentally verify the effectiveness and the edge detection capability of the designed metasurface, the fabricated metasurface sample and imaging experimental are shown in **Figure 4**. As shown in Figure 4a, the experimental metasurface sample is fabricated by reactive ion etching (RIE) process and electron beam lithography (EBL) on a glass substrate (for details of the sample fabrication, see Methods and Section S8, Supporting Information). The top view and side view of the SEM images of the metasurface are shown in Figure 4b,c, respectively, which shows a good performance of fabrication.

Next, we employ the experimental setup depicted in Figure 4d to illustrate the edge detection capabilities of our fabricated metasurface sample. The main components of the experimental setup are the incident source, half-wave plate, imaging target, the nonlocal hollow metasurface sample, microscope objective, and magnified imaging system consisting of a tube lens and an infrared camera (CIS-CM990) that can efficiently capture images in the near-infrared region, respectively. Among them, a supercontinuum laser (NKT Photonics Superk EVO) provides an incident light source with polarization characteristics. The polarization direction of the incident beam can be modified by adding the half-wave plate in front of the detection target. In the experiment, we place the metasurface differentiator at an appropriate distance behind the target so that the differentiator can better filter the incident wave vectors in different directions of the target image. More importantly, during the experiments, we performed precise positioning and calibration of the sample and lens imaging quality to minimize experimental misalignments to the greatest extent possible. Additionally, to quantitatively evaluate the efficiency of edge detection using our nonlocal hollow metasurface, a quantitative metric between the intensity of the filtered output image and the input image is essential. For this purpose, we have adopted the *peak efficiency* (η_{peak}) from Ref.[53] as a quantitative metric to assess the actual efficiency. The peak efficiency is defined as the ratio of the maximum output intensity to the peak intensity of the input image, which can be clearly represented using calibrated color bars. This approach allows us to provide a more precise and intuitive evaluation of the device's performance in edge detection tasks.

To begin with, the photographs of a dog and a dove with irregular edges profile are used as input images for the *x*- and *y*-polarized illumination at wavelengths of 1350 and 1285 nm, as shown in Figure 4e,h, respectively. As the nonlocal hollow metasurface Laplace differentiator is added to the experimental process, the edge detection results can be immediately captured and

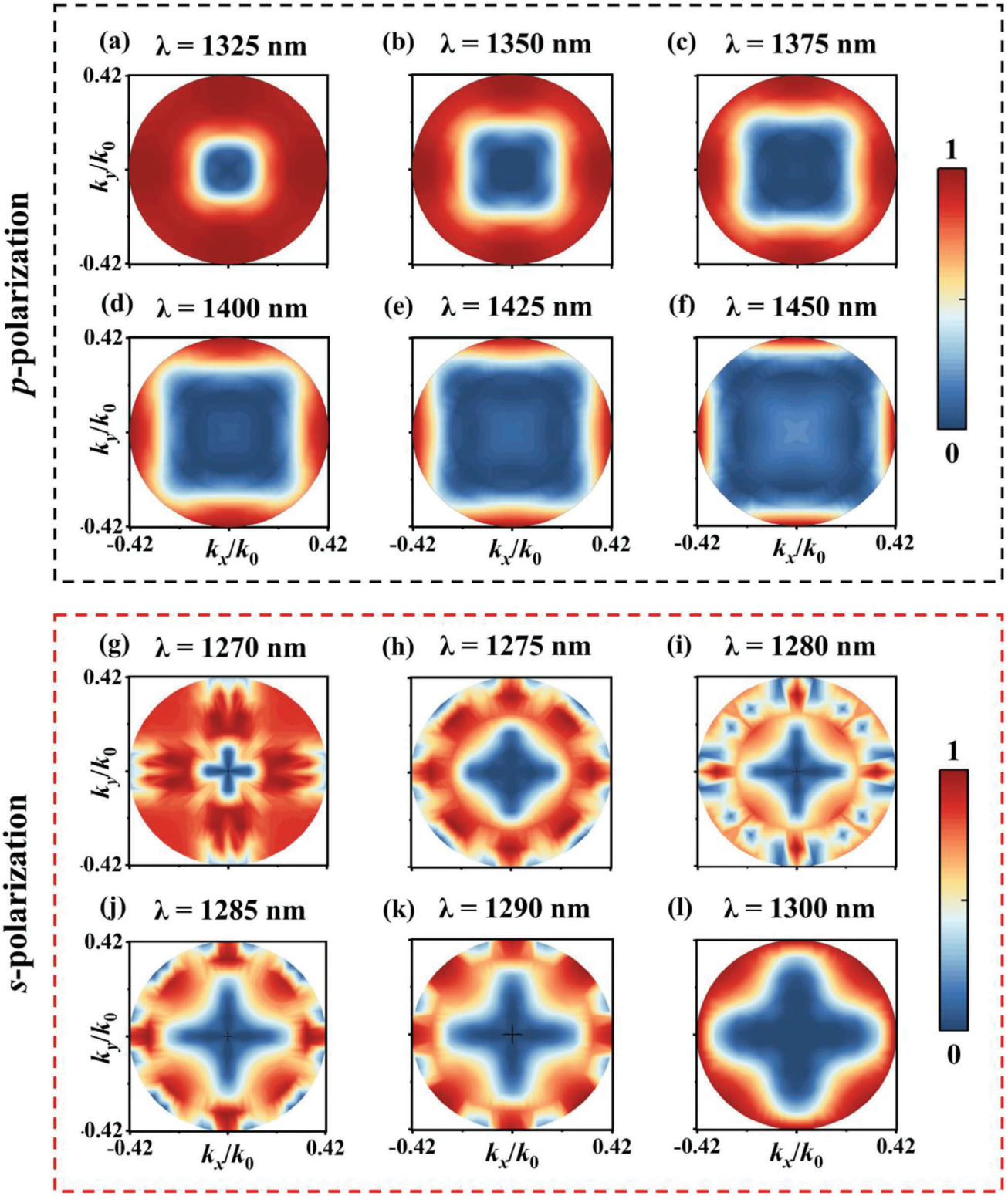

Figure 3. 2D dispersive behaviors of the nonlocal hollow metasurface for *p*- and *s*-polarized incidence at different wavelength ranges. a–f) and g–l) are the angularly distributed transmittance amplitude of the metasurface for *p*- and *s*-polarized conditions for incidence within 0° to 25° (corresponding to $k_x/k_0 = \pm 0.42$), respectively.

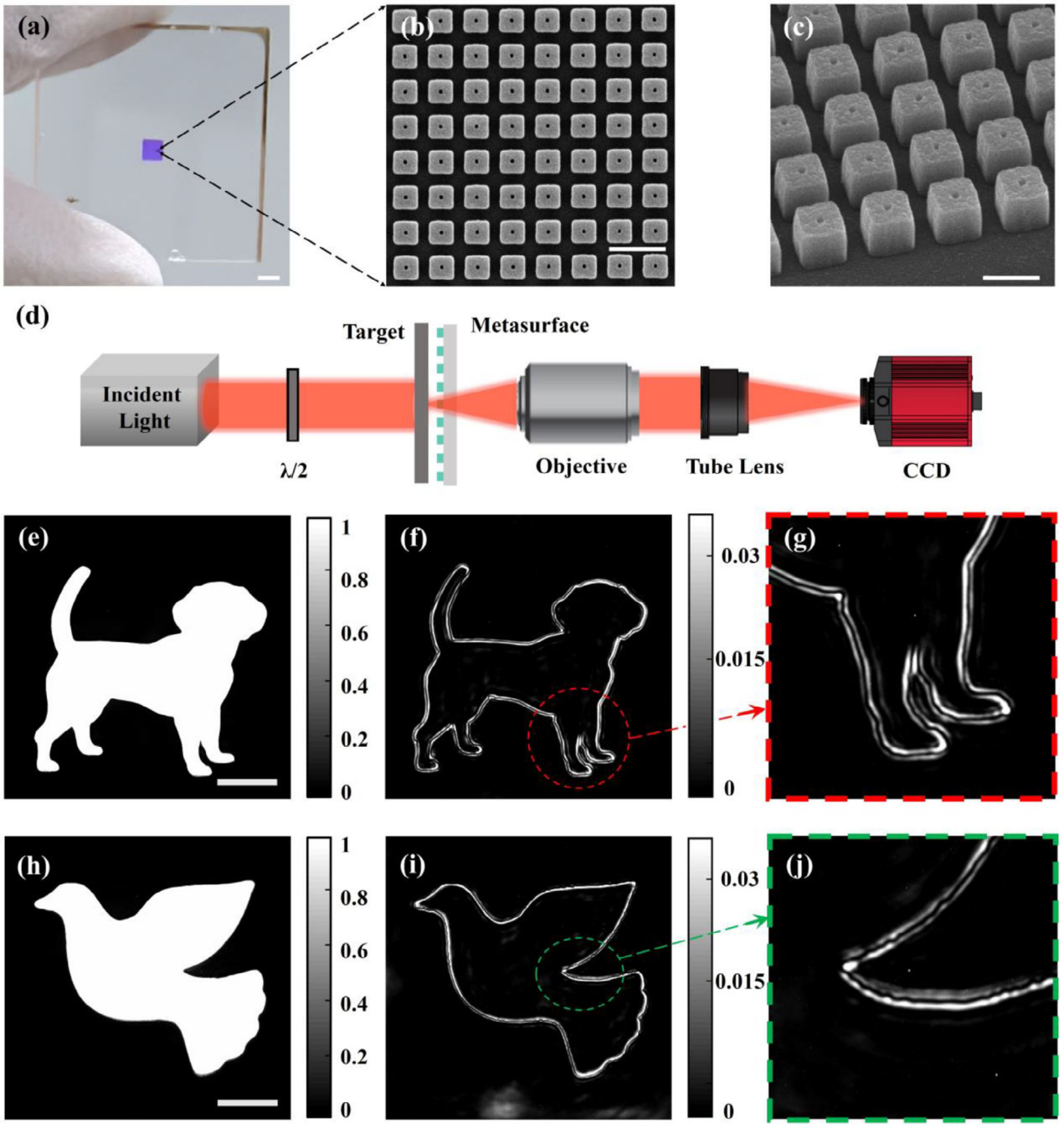

Figure 4. The nonlocal hollow metasurface sample and imaging experiment. a) Photograph of the sample. Metasurface patterened area, 900 μm × 900 μm. Scale bar, 1 mm. b,c) Scanning electron microscopy images in top and side views of the fabricated nonlocal hollow metasurface sample with scales of 1 and 500 nm, respectively. d) The experimental setup for edge detection imaging. The half-wave plate is used to manipulate the polarization of the incident light. The lens images the back focal plane of the microscope objective (20x/0.6) to a CCD camera. e,f) and h,i) Results of imaging about the pictures of dog and dove without and with the metasurface differentiator in the case of *x*- and *y*-polarized in 1350 and 1285 nm, respectively. Scale bar, 200 μm. g,j) Enlarged details of parts in (f) and (i).

easily observed as shown in Figure 4f,i, respectively. To more clearly observe the images processed by this Laplace metasurface differentiator, a portion of the local contours of the dog and dove in Figure 4f,i are randomly selected and magnified to enhance the details and inspection, as shown in Figure 4g,i, respectively. Obviously, two closely adjacent solid line contours indeed form around the edges of the target patterns. The real-time recording of the edge detection results of "dog" and "dove" are provided in Video S1 and Video S2 (Supporting Information), respectively. This observation is sufficient to validate the effective-

ness of the designed nonlocal metasurface Laplace differentiator can directly achieve 2D second-order edge detection in the spatial space with dual polarization channels for target objects without 4*f* system.

2.6. Experimental Results for Broadband and Dual-Polarized Edge Detection

Additionally, besides the Laplacian differentiation that can be achieved at 1350 nm in the *x*-polarization and 1285 nm in the *y*-polarization, the nonlocal hollow metasurface can also exhibit broadband characteristics in dual-polarization channels. This is attributed to the fact that the designed silicon hollow structure excites Q-BIC-1 and Q-BIC-2 resonance modes in the *p*-polarization and *s*-polarization channels, respectively. These resonance modes lead to the gradual broadening of the transmission spectrum as the oblique incidence angle increases. Consequently, a certain operational bandwidth can be obtained near the resonance position. This can also be observed from the transmission spectra shown in Figure 2b,c. Simultaneously, in Figure 3, we analyze the broadband isotropic performance of the nonlocal hollow metasurface differentiator, which can also demonstrate this point. Therefore, even when deviating from the designed wavelength position in dual-polarization channels, the metasurface differentiator can still be regarded as an imperfect Laplacian operator at these wavelengths. Next, we continue to use the images of the dog and dove in Figure 4e,f to prove the broadband 2D second-order edge detection in dual-polarization channels.

Under *x*- and *y*-polarized illumination, the input images are tested for broadband edge detection, as depicted in **Figure 5**. For the *x*-polarized channel case, from 1285 to 1450 nm, the nonlocal hollow metasurface Laplacian differentiator can essentially exhibit clear 2D second-order edge detection. The corresponding results are shown in Figure 5a. However as the wavelength increases, at 1425 nm in the *x*-polarized channel, the wave vectors of the incident waves at small angles cannot be completely filtered out by the metasurface differentiator, resulting in a nonzero smaller value of the transmission spectrum amplitude. This can result in a small portion of low-frequency information in the image not being filtered out, ultimately appearing in the edge detection results. Nevertheless, the majority of high-frequency information in the image still passes through the nonlocal hollow metasurface smoothly, allowing for the observation of clear edge and contour features. This trend can be clearly observed by comparing the normalized intensity distributions at the same locations(the green dashed line) in the dog images shown in Figures 4e,f and 5a. Within the range from 1285 to 1450 nm, two close peaks formed around each edge of the target image, as depicted in Figure 5c. Compared to the edge detection results under *y*-polarization shown in Figure 5b from 1270 nm to 1300 nm, *x*-polarization can support 2D second-order edge detection over a broadband range approaching 165 nm, which is equivalent to five times the broadband range under *y*-polarization. However, while the broadband operating range for Laplacian differentiation in the *y*-polarized channel is not as extensive as that in the *x*-polarized channel, the *y*-polarized channel can still maintain a stable and complete 2D second-order edge detection of the image spanning a 30 nm range. This trend can also be clearly observed by comparing the normalized intensity distributions at the same locations in the dove images shown in Figures 4h,i and 5b. Within the range from 1270 to 1300 nm at the edges of the target image, two closely spaced peaks are always formed, as depicted in Figure 5d. Additionally, from the experimental results of the cropped sections of the dog and dove patterns in Figure 5c,d, it is not difficult to observe that the edge detection effect is quite distinct. Consequently, these experimental results provide ample evidence that the metasurface is indeed capable of performing broadband Laplacian differential operations and 2D second-order edge detection in both orthogonal polarization channels.

Furthermore, to experimentally quantify resolution, we utilized our nonlocal hollow metasurface device to detect the edge imaging effects on the sixth and seventh groups of the 1951 USAF resolution test chart under *x*-polarized light at 1425 nm and *y*-polarized light at 1300 nm, respectively (for details, see Section S6, Supporting Information). The experimental results demonstrate that the elements in the seventh group also exhibit edge detection effects under 1425 nm *x*-polarized and 1300 nm *y*-polarized, respectively. It indicates that the spatial differentiation resolution of our designed nonlocal hollow metasurface in 2D space can reach up to 2.19 μm, corresponding to the sixth element of the seventh group.

2.7. Broadband and Dual-Polarized Edge Detection for Biological Cells

Generally speaking, image edge detection techniques play a significant role in the field of biomedicine. For instance, cell detection and feature extraction are crucial for enhancing the speed and accuracy of diagnostics, which is of great importance for disease diagnosis and treatment. As a confirmatory experiment, we employ the designed nonlocal hollow metasurface differentiator device to conduct experimental validation for the identification of onion epidermal cells, pumpkin vesicular tissue, capsicum peel cells, and a portion of the fly wing.

As depicted in **Figure 6**a–d, without the incorporation of our metasurface differentiator, it is not possible to directly distinguish onion epidermal cells, pumpkin vesicular tissue, capsicum peel cells, and a portion of fly wing illuminated by *x*-polarized light at 1350 nm within the visual field. Among them, the complete fly wing of Figure 6d can be seen in Section S7 in Supporting Information. After introducing our designed metasurface differentiator, the edges and contours of those biological cells can be observed quickly and clearly in Figure 6e–h–l, under 1350 nm *x*-polarized and 1285 nm *y*-polarized, respectively. Hence, the nonlocal hollow metasurface differentiator designed in this work, capable of performing broadband Laplacian differential operations with a large NA in dual polarization cases, will allow transparent cells to be easily identified, greatly facilitating the observation of cell morphology and behavioral patterns in biological research. Furthermore, integrating this image edge detection technology into the field of biomedical imaging field, such as in endoscope systems, could significantly enhance the accuracy of image analysis and diagnostic efficiency for medical professionals in the future.

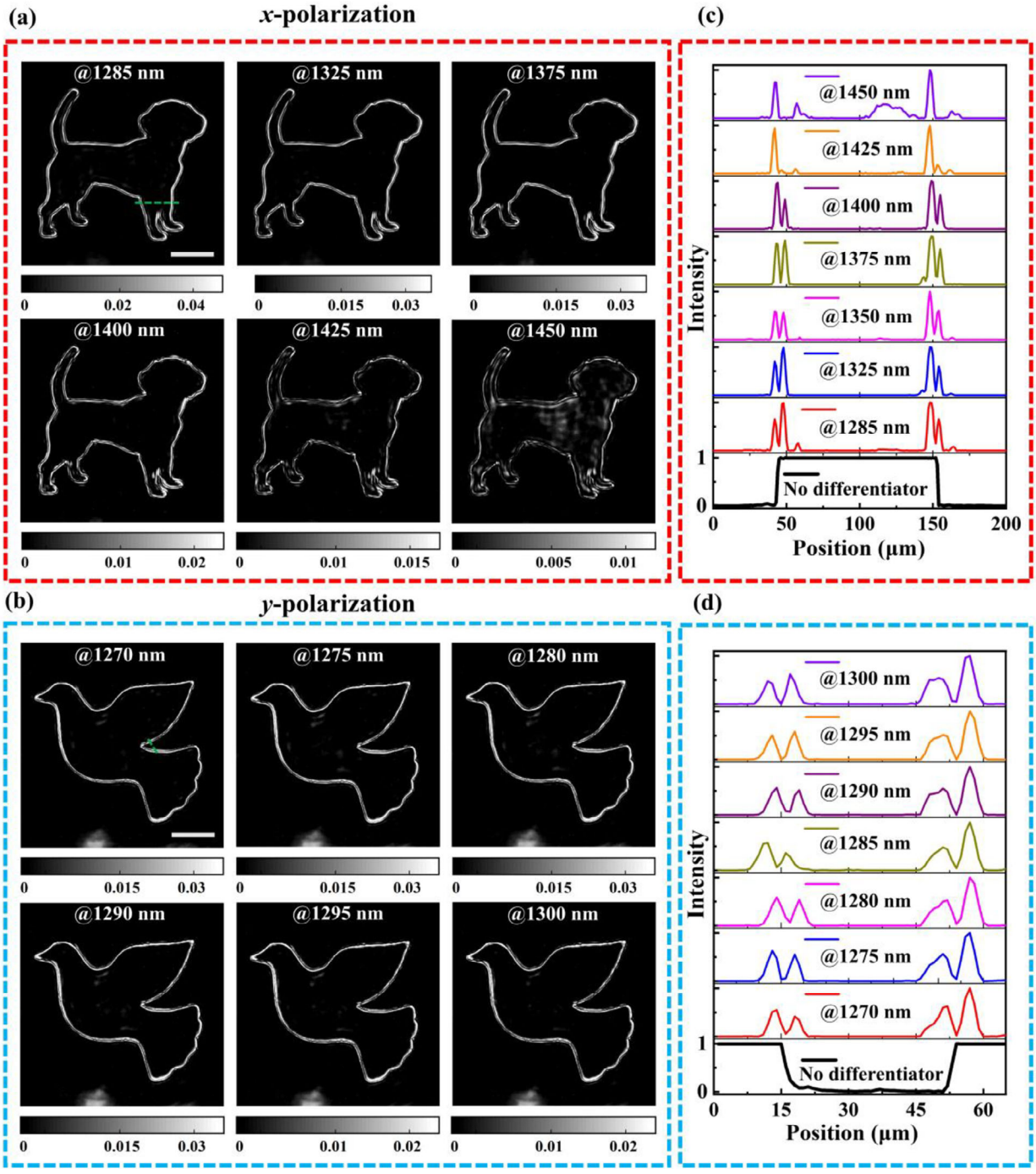

Figure 5. Dual-polarized broadband edge detection with nonlocal hollow metasurface differentiator. A,b) Edge detection results under *x*- and *y*-polarized at different wavelengths with the nonlocal hollow metasurface differentiator for the dog and dove in Figure 4e,h), respectively. c,d) Normalized intensity contrasts corresponding to the cut line positions *x*- and *y*-polarized at different wavelengths in Figure 5a,b), respectively. Among them, the cut lines for "no differentiator" and "1350 nm " in Figure 5c) are derived from Figure 4e,f), and the cut line for "no differentiator" and "1285 nm" in Figures 5d) are taken from Figure 4h,i. Scale bar, 200 μm.

3. Conclusion

In conclusion, we theoretically propose and experimentally demonstrate a simple geometrically shaped, easily mass-producible single-layer nonlocal hollow metasurface differentiator. This metasurface differentiator is capable of exciting different Q-BIC modes, manifesting as magnetic dipole resonance and magnetic quadrupole resonance with incident angle dependence under *p*- and *s*-polarized illumination, respectively. This provides the necessary foundation for the optical transfer

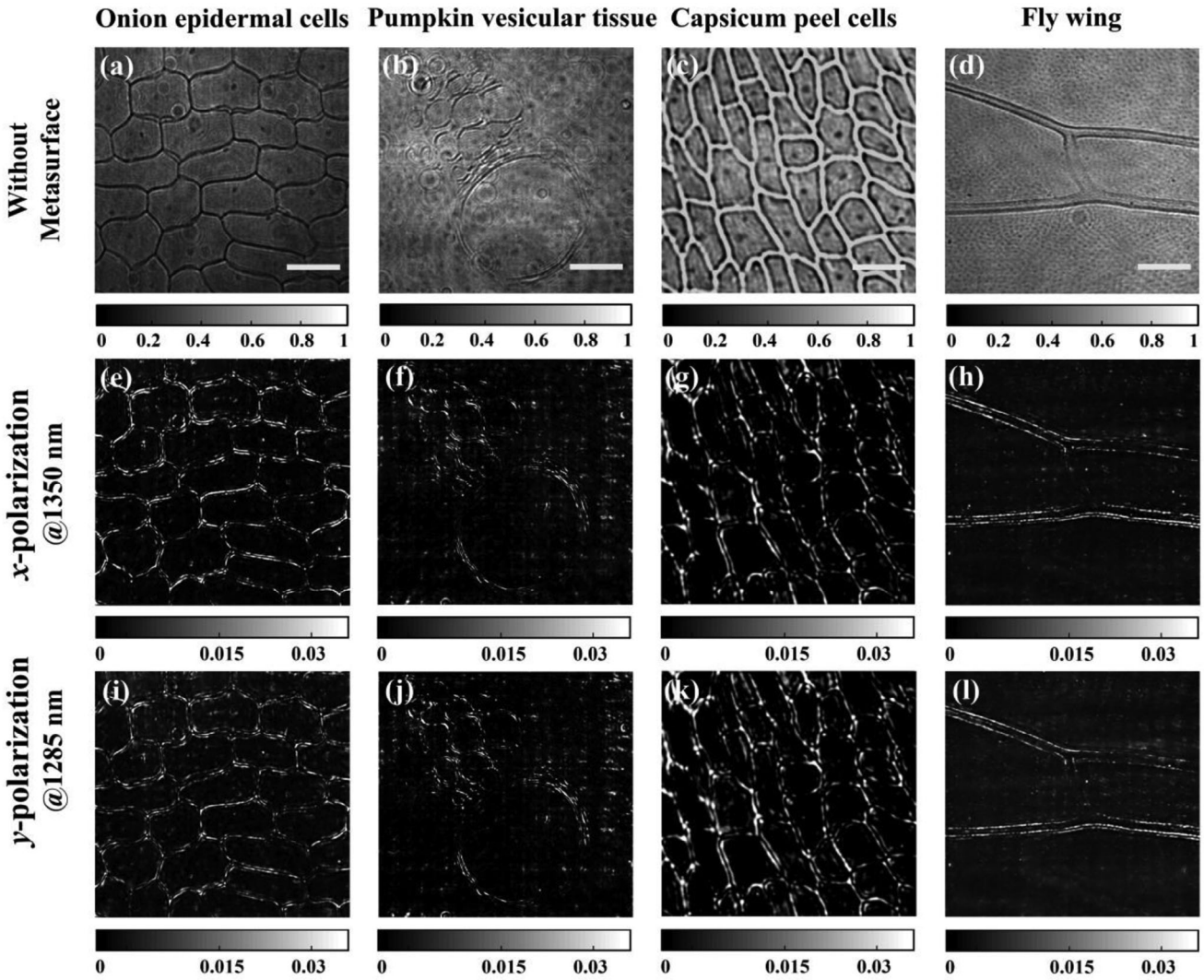

Figure 6. Experimental results of imaging biological cells by using nonlocal hollow metasurface differentiators. a–d) Imaging of onion epidermal cells, pumpkin vesicular tissue, capsicum peel cells, and a portion of fly wings under 1350 nm *x*-polarized without the metasurface differentiators. All the scale bars are 40 μm. e–h) and i–l) Edge detection results of the biological cells with the metasurface differentiators correspond to those in Figure a–d) under 1350 nm *x*-polarized and 1285 nm *y*-polarized, respectively.

function to fulfill the requirements of the Laplacian differential operator in dual-polarization channels. In practical experiments, the broadband range for performing high-quality, large NA, and 2D second-order edge detection on images achieves 165 and 30 nm in the *x*-polarization and *y*-polarization channels, respectively. Compared to traditional 4*f* filtering systems, the dual-polarization nonlocal hollow metasurface differentiator designed in this work can directly implement compact, low-power, and ultra-fast optical analog computation and image processing in real space. This advancement offers strong support for the development of advanced imaging instruments. For instance, it can be seamlessly integrated with existing commercial imaging systems, such as microscopes, demonstrating significant potential for future applications in autonomous driving, machine vision, and biomedical imaging. Moreover, we anticipate that inverse design and other more advanced methods can be employed to achieve more complex nonlocal responses in metasurface, which is expected to enable a greater variety of optical transfer functions and more advanced optical analog computations, as well as an enriched capacity for image processing.

4. Experimental Section

Simulations: The transmission spectra in Figure 2b,c are calculated using the Finite differential time domain method. For the unit cell simulation, the plane wave sources come from the substrate side and with the propagation direction of +z are placed inside the SiO2 substrate. The periodic boundary conditions (PBC) are used along the *x* and *y* axes. Meanwhile, perfectly matched layers (PMLs) are added at the top and bottom as the boundaries along the axis. The transmitted fields are recorded from a field monitor that is placed above the structures.

The electromagnetic modes profiles in Figure 2d–g are simulated using the Finite element method. PMLs are added at the top and bottom of the structure. PBC are applied in the x and y directions to simulate the periodic

unit cell. The in-plane wavevector is swept along the Γ–X direction. The refractive index of silica substrate is 1.45.

Sample Fabrication: Our designed nonlocal hollow metasurface differentiator is fabricated on a fused quartz substrate by utilizing electron beam lithography (EBL) and reactive ion etching (RIE). First, a 450 nm thick amorphous silicon (α-Si) film is deposited by the plasma-enhanced chemical vapor deposition (PECVD) method. Then, a PMMA electron beam resist (EBR) of 300 nm is spinning coated onto Si substrate. The desired structure is patterned by utilizing JEOL 6300FS EBL at a base dose of 1000 μC cm^{-2} with an accelerating voltage of 150 kV. After the exposure process, the resist is developed in 1:3 MIBK:IPA solution for 40 s and rinsed in IPA for 30 s successively, followed by a deposition of 80 nm Cr using the electron beam evaporation deposition (EBD) method. To realize the lift-off process, the sample is immersed in hot acetone of 65 °C and cleaned by ultrasonic. Finally, by using inductively coupled plasma reactive ion etching (RIE) method with HBr at room temperature (RT) for 180 s (flow rate of 50 sccm, pressure of 10 mTorr, RF, and ICP power of 50 and 750 W, respectively), the desired structure is transferred from Cr to silicon and the remaining Cr is removed by cerium (IV) ammonium nitrate. Additionally, we perform simulation analyses to investigate the impact of etching errors in the central holes during the fabrication of the metasurface samples on the resonant properties of the device, as detailed in Section S9 (Information Section).

Supporting Information

Supporting Information is available from the Wiley Online Library or from the author.

Acknowledgements

The authors acknowledge the funding provided by the National Key R&D Program of China (2021YFA1401200), the National Natural Science Foundation of China (No. U21A20140) program, and the Beijing Natural Science Foundation (JQ24028).

Conflict of Interest

The authors declare no conflict of interest.

Data Availability Statement

The data that support the findings of this study are available from the corresponding author upon reasonable request.

Keywords

edge detection, laplace differentiator, metasurface, quasi-bound states in the continuum

Received: December 31, 2024
Revised: March 16, 2025
Published online: April 17, 2025

[1] P. Ambs, *Adv.Opt. Technol.* **2010**, *2010*, 372652.
[2] R. J. Martins, E. Marinov, M. A. B. Youssef, C. Kyrou, M. Joubert, C. Colmagro, V. Gâté, C. Turbil, P. M. Coulon, D. Turover, S. Khadir, M. Giudici, C. Klitis, M. Sorel, P. Genevet, *Nat. Commun.* **2022**, *13*, 5724.
[3] D. Liang, C. Zhang, P. Zhang, S. Liu, H. Li, S. Niu, R. Z. Rao, L. Zhao, X. Chen, H. Li, Y. Huo, *Nat. Commun.* **2024**, *15*, 7660.
[4] E. Marinov, R. J. Martins, M. A. B. Youssef, C. Kyrou, P.-M. Coulon, P. Genevet, *Adv. Photon.* **2023**, 5.
[5] Y. Kim, G. Lee, J. Sung, J. Jang, B. Lee, *Adv. Funct. Materials* **2022**, *32*, 2106050.
[6] L. Wesemann, J. Rickett, J. Song, J. Lou, E. Hinde, T. J. Davis, A. Roberts, *Light Sci. Appl.* **2021**, *10*, 98.
[7] C. Xu, R. Zhao, X. Zhang, S. Zhang, X. Li, G. Geng, J. Li, X. Li, Y. Wang, L. Huang, *eLight* **2024**, *4*, 9.
[8] Y. Gan, J. Xiao, T. Plaskocinski, S. Persheyev, M. Biabanifard, A. Di Falco, *Laser & Photonics Reviews* **2024**, 2401240.
[9] M. Gopakumar, G. Y. Lee, S. Choi, B. Chao, Y. Peng, J. Kim, G. Wetzstein, *Nature* **2024**, *629*, 791.
[10] A. Silva, F. Monticone, G. Castaldi, V. Galdi, A. Alù, N. Engheta, *Science* **2014**, *343*, 160.
[11] T. Badloe, S. Lee, J. Rho, *Adv. Photon.* **2022**, 4.
[12] J. W. Goodman, *Introduction to Fourier Optics*, Roberts and Company Publishers, Englewood, CO, **2005**.
[13] S. Abdollahramezani, A. Chizari, A. E. Dorche, M. V. Jamali, J. A. Salehi, *Opt. Lett.* **2017**, *42*, 1197.
[14] W. Ji, J. Chang, H.-X. Xu, J. R. Gao, S. Gröblacher, H. P. Urbach, A. J. L. Adam, *Light Sci Appl* **2023**, *12*, 169.
[15] B. Leng, Y. Zhang, D. P. Tsai, S. Xiao, L. A. Manuf, *Light Adv. Manuf.* **2024**, *5*, 117.
[16] W. Yang, J. Zhou, D. P. Tsai, S. Xiao, *Photonics Insights* **2024**, *3*, R04.
[17] K. Du, H. Barkaoui, X. Zhang, L. Jin, Q. Song, S. Xiao, *Nanophotonics* **2022**, *11*, 1761.
[18] N. Yu, P. Genevet, M. A. Kats, F. Aieta, J. P. Tetienne, F. Capasso, Z. Gaburro, *Science* **2011**, *334*, 333.
[19] A. V. Kildishev, A. Boltasseva, V. M. Shalaev, *Science* **2013**, *339*, 1232009.
[20] N. Yu, F. Capasso, *Nature Mater* **2014**, *13*, 139.
[21] L. Huang, S. Zhang, T. Zentgraf, *Nanophotonics* **2018**, *7*, 1169.
[22] S. C. Malek, A. C. Overvig, A. Alù, N. Yu, *Light Sci. Appl.* **2022**, *11*, 246.
[23] J.-H. Song, J. Van De Groep, S. J. Kim, M. L. Brongersma, *Nat. Nanotechnol.* **2021**, *16*, 1224.
[24] Z. Wang, S. Wan, C. Dai, Z. Li, Z. Li, *Adv. Funct. Materials* **2024**, 2415823.
[25] B. Wu, W. Jiang, J. Jiang, Z. Zhao, Y. Tang, W. Zhou, W. Chen, *Adv. Funct. Materials* **2024**, *34*, 2316745.
[26] R. Zhao, B. Sain, Q. Wei, C. Tang, X. Li, T. Weiss, L. Huang, Y. Wang, T. Zentgraf, *Light Sci. Appl.* **2018**, *7*, 95.
[27] R. Zhao, L. Huang, Y. Wang, *PhotoniX* **2020**, *1*, 20.
[28] X. Jing, R. Zhao, X. Li, Q. Jiang, C. Li, G. Geng, J. Li, Y. Wang, L. Huang, *Nat. Commun.* **2022**, *13*, 7842.
[29] Y. Xu, X. Su, Z. Chai, J. Li, *Laser Photonics Rev.* **2024**, *18*, 2300355.
[30] N. Feldman, K. M. M. Goeloe, A. J. Den Boef, L. V. Amitonova, A. F. Koenderink, *ACS Photonics* **2024**, *11*, 5229.
[31] X. Ding, Z. Wang, G. Hu, J. Liu, K. Zhang, H. Li, B. Ratni, S. N. Burokur, Q. Wu, J. Tan, C. W. Qiu, *PhotoniX* **2020**, *1*, 16.
[32] F. Zangeneh-Nejad, D. L. Sounas, A. Alù, R. Fleury, *Nat. Rev. Mater.* **2020**, *6*, 207.
[33] X. Wang, H. Hao, X. He, P. Xie, J. Liu, J. Tan, H. Li, H. Wang, P. Genevet, Y. Luo, X. Ding, G. Hu, *Nat. Rev. Electr. Eng.* **2024**, *1*, 391.
[34] T. Zhu, Y. Zhou, Y. Lou, H. Ye, M. Qiu, Z. Ruan, S. Fan, *Nat. Commun.* **2017**, *8*, 15391.
[35] T. Zhu, Y. Lou, Y. Zhou, J. Zhang, J. Huang, Y. Li, H. Luo, S. Wen, S. Zhu, Q. Gong, M. Qiu, Z. Ruan, *Phys. Rev. Applied* **2019**, *11*, 034043.
[36] J. Zhou, H. Qian, C.-F. Chen, J. Zhao, G. Li, Q. Wu, H. Luo, S. Wen, Z. Liu, *Proc. Natl. Acad. Sci. U.S.A.* **2019**, *116*, 11137.
[37] R. C. Gonzalez, R. E. Woods, *Digital Image Processing*, 3rd ed., Prentice Hall, Upper Saddle River, NJ, USA, **2008**.

[38] H. Kwon, D. Sounas, A. Cordaro, A. Polman, A. Alù, *Phys. Rev. Lett.* **2018**, *121*, 173004.
[39] C. Guo, M. Xiao, M. Minkov, Y. Shi, S. Fan, *Optica* **2018**, *5*, 251.
[40] Y. Liang, D. P. Tsai, Y. Kivshar, *Phys. Rev. Lett.* **2024**, *133*, 053801.
[41] C. Guo, M. Xiao, M. Minkov, Y. Shi, S. Fan, *J. Opt. Soc. Am. A* **2018**, *35*, 1685.
[42] M. Kim, D. Lee, J. Kim, J. Rho, *Laser Photonics Rev.* **2024**, *18*, 2300718.
[43] Y. Zhou, H. Zheng, I. I. Kravchenko, J. Valentine, *Nat. Photonics* **2020**, *14*, 316.
[44] A. Cordaro, H. Kwon, D. Sounas, A. F. Koenderink, A. Alù, A. Polman, *Nano Lett.* **2019**, *19*, 8418.
[45] Z. Dong, J. Si, X. Yu, X. Deng, *Appl. Phys. Lett.* **2018**, *112*, 181102.
[46] A. Komar, R. A. Aoni, L. Xu, M. Rahmani, A. E. Miroshnichenko, D. N. Neshev, *ACS Photonics* **2021**, *8*, 864.
[47] A. Roberts, D. E. Gómez, T. J. Davis, *J. Opt. Soc. Am. A* **2018**, *35*, 1575.
[48] L. Wan, D. Pan, S. Yang, W. Zhang, A. A. Potapov, X. Wu, W. Liu, T. Feng, Z. Li, *Opt. Lett.* **2020**, *45*, 2070.
[49] D. Pan, L. Wan, M. Ouyang, W. Zhang, A. A. Potapov, W. Liu, Z. Liang, T. Feng, Z. Li, *Photon. Res.* **2021**, *9*, 1758.
[50] X. Zhang, B. Bai, H. Sun, G. Jin, J. Valentine, *Laser Photonics Rev.* **2022**, *16*, 2200038.
[51] Y. Zhou, W. Wu, R. Chen, W. Chen, R. Chen, Y. Ma, *Adv. Opt. Mater.* **2020**, *8*, 1901523.
[52] H. Kwon, A. Cordaro, D. Sounas, A. Polman, A. Alù, *ACS Photonics* **2020**, *7*, 1799.
[53] M. Cotrufo, A. Arora, S. Singh, A. Alù, *Nat. Commun.* **2023**, *14*, 7078.
[54] M. Cotrufo, S. Singh, A. Arora, A. Majewski, A. Alù, *Optica* **2023**, *10*, 1331.
[55] C. W. Hsu, B. Zhen, A. D. Stone, J. D. Joannopoulos, M. Soljačić, *Nat. Rev. Mater.* **2016**, *1*, 16048.
[56] Y. Chen, H. Deng, X. Sha, W. Chen, R. Wang, Y.-H. Chen, D. Wu, J. Chu, Y. S. Kivshar, S. Xiao, C.-W. Qiu, *Nature* **2023**, *613*, 474.
[57] A. C. Valero, H. K. Shamkhi, A. S. Kupriianov, T. Weiss, A. A. Pavlov, D. Redka, V. Bobrovs, Y. Kivshar, A. S. Shalin, *Nat. Commun.* **2023**, *14*, 4689.
[58] Y. Zeng, X. Zhang, X. Ouyang, Y. Li, C. Qiu, Q. Song, S. Xiao, *Adv. Opt. Mater.* **2024**, *12*, 2400296.
[59] Y. Liang, K. Koshelev, F. C. Zhang, H. Lin, S. R. Lin, J. Y. Wu, B. H. Jia, Y. Kivshar, *Nano Lett.* **2020**, *20*, 6351.
[60] Y. Tang, Y. Liang, J. Yao, M. K. Chen, S. Lin, Z. Wang, J. Zhang, X. G. Huang, C. Yu, D. P. Tsai, *Laser Photonics Rev.* **2023**, *17*, 2200597.
[61] H. M. Doeleman, F. Monticone, W. den Hollander, A. Alù, A. F. Koenderink, *Nat. Photon.* **2018**, *12*, 397.
[62] K. Koshelev, S. Lepeshov, M. Liu, A. Bogdanov, Y. Kivshar, *Phys. Rev. Lett.* **2018**, *121*, 193903.
[63] H. H. Hsiao, A. Y. Liu, J. C. Hsieh, Y. H. Lin, *Adv. Opt. Mater.* **2022**, *10*, 2200812.
[64] H. H. Hsiao, J. C. Hsieh, A. Y. Liu, K. I. Lin, Y. C. Hsu, *Nanophotonics* **2024**, *13*, 3155.
[65] M. Zhou, S. You, J. Liu, K. Qin, J. Wang, Y. Zhang, H. Xiang, C. Zhou, D. Han, *ACS Photonics* **2024**, *11*, 2413.
[66] R. N. Bracewell, *The Fourier Transform and its Applications*, 3rd ed., McGraw-Hill, New York, USA, **2000**.